THE JOURNAL OF PHYSICAL CHEMISTRY LETTERS
A JOURNAL OF THE AMERICAN CHEMICAL SOCIETY

pubs.acs.org/JPCL

Letter

Coupling between Emissive Defects on Carbon Nanotubes: Modeling Insights

Braden M. Weight, Andrew E. Sifain, Brendan J. Gifford, Dmitri Kilin, Svetlana Kilina, and Sergei Tretiak*

Cite This: *J. Phys. Chem. Lett.* 2021, 12, 7846–7853

Read Online

ACCESS | Metrics & More | Article Recommendations | Supporting Information

ABSTRACT: Covalent functionalization of single-walled carbon nanotubes (SWCNTs) with organic molecules results in red-shifted emissive states associated with sp^3-defects in the tube lattice, which facilitate their improved optical functionality, including single-photon emission. The energy of the defect-based electronic excitations (excitons) depends on the molecular adducts, the configuration of the defect, and concentration of defects. Here we model the interactions between two sp^3-defects placed at various distances in the (6,5) SWCNT using time-dependent density functional theory. Calculations reveal that these interactions conform to the effective model of J-aggregates for well-spaced defects (>2 nm), leading to a red-shifted and optically allowed (bright) lowest energy exciton. H-aggregate behavior is not observed for any defect orientations, which is beneficial for emission. The splitting between the lowest energy bright and optically forbidden (dark) excitons and the pristine excitonic band are controlled by the single-defect configurations and their axial separation. These findings enable a synthetic design strategy for SWCNTs with tunable near-infrared emission.

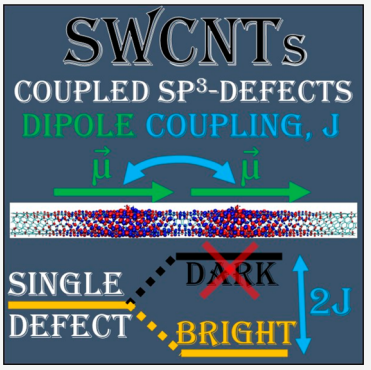

Recent success in controlling the features and dynamics of excitonic states in single walled carbon nanotubes (SWCNTs) has led to advances in surface functionalization techniques to overcome low emission capacity inherent to pristine (i.e., defect-free) SWCNTs.[1−8] Functionalization of the SWCNT surface by small organic molecules at low concentrations introduces sp^3-hybridized defects that spatially localize the low-energy excited state electronic wave functions. These new states are optically allowed (bright) and are able to capture rapidly diffusing excitons characteristic for pristine SWCNTs, which altogether dramatically increases photoluminescence (PL) efficiency centered in the near-infrared spectral region.[2,4,9−15] These features make functionalized SWCNTs promising materials for highly tunable single-photon emitters operating in the telecom relevant wavelengths at room temperature,[9,16−18] which is a key element of any quantum photonic circuit needed for quantum information processing.[19] However, the resulting emission energies are dependent both on the chemical composition of the adduct and on the defect binding configuration.[9−11,14] Recent computational reports have demonstrated that the latter plays the dominant role in the PL characteristics related to defect-localized states.[11,14,20,21] However, controlling precise binding configurations is a challenge for currently developed chemical means such as aryl diazonium chemistry[13,22] or photochemistry.[23]

In experimental spectra of chemically functionalized SWCNTs, there are typically two prominent defect-associated emission bands, labeled as E_{11}^* and E_{11}^{*-} (or E** in some reports), each red-shifted from the E_{11} band being the emission peak in pristine systems.[13,15,20,23] Typically, these two bands correspond to different defect configurations.[9−11,22] The range of available binding configurations acts as a source for broadening the span of observed emission wavelengths and diversity of the emission features in low-temperature single-tube emission experiments.[17,18,22,24] As such, new reactive schemes are needed for refined control over the defect configuration, which will allow for defining a narrow band of emission at the targeting wavelength.[25] Moreover, the route toward this includes not only control over the local binding configuration, but also one needs to resolve the role of the local chemical environment and interactions between closely spaced sp^3-defects.[22] Recent experiments have introduced methods, such as high-resolution single-defect spectroscopy[26] and utilization of chemical reactions with a single-stranded DNA exposed to singlet oxygen,[27,28] to pattern and examine spatially localized and interacting defects. These studies leave many open questions regarding the strength of coupling (i.e., electrostatic interactions) between sp^3-defects, which can be modulated by both the defect binding configuration and their separation/arrangement on the SWCNT surface.

For both pristine and functionalized SWCNTs, the concept of exciton size has been extensively studied.[1,5−7,29−35] The

Received: June 1, 2021
Accepted: July 15, 2021
Published: August 12, 2021

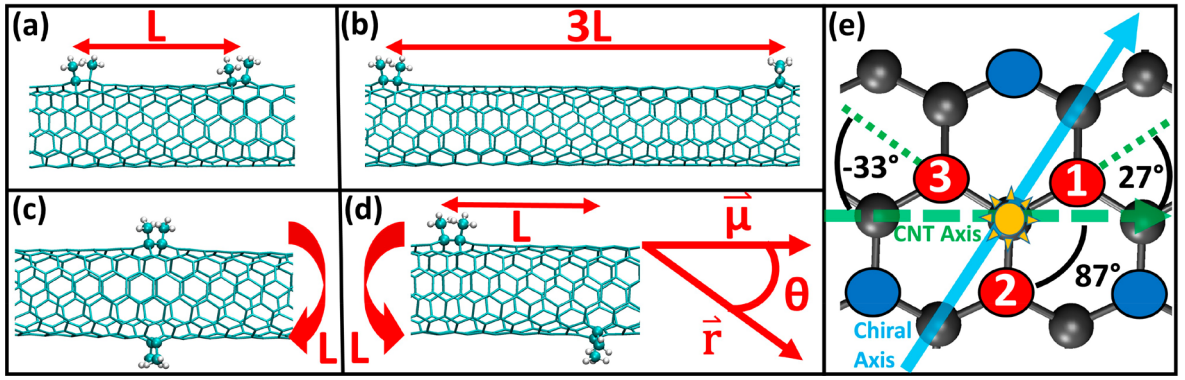

Figure 1. Optimized structures of the (6,5) nanotube functionalized by four methyl groups resulting in a pair of sp^3-defects of various configurations. We consider only pairs of *ortho* (1, 2, and 3) defects separated from each other by different distances scaled by L, which is defined as 10 separating carbons (~1.3 nm) and is equivalent to half of the circumference: (a) Axial L (AxL) for C_{11} defects, (b) Axial 3L (Ax3L)for C_{23} defects, (c) Circumferential L (CircL) for C_{12} defects, (d) Axial L Circumferential L (AxL/CircL) for C_{12} defects, and (e) definition of all single-defect configurations: possible ways of creating a single sp^3-defect, with three *ortho* (red circles) and three *para* (blue circles) types.

redshift in emission energy in low-lying defect-associated excited states correlates well to increased localization of the wave function due to a one-dimensional effective potential well created by the defect.[11,15,20,22] In the case of multiple interacting sp^3-defects, the exciton may be shared in a nontrivial way between each defect site,[28] either exhibiting a more delocalized nature across both sites or localization to a single defect. The resulting excitonic properties will depend on the defect−defect coupling strength, presumably varying with defect binding configuration, composition, placement, and separation length (see Figure 1a−d).

In this work, we investigate interacting and localized excitonic states stemming from a pair of covalent sp^3-hybridized defects on the surface of an experimentally relevant (6,5) SWCNT in the framework of an effective Frenkel Exciton Hamiltonian model[36,37] (Scheme 1) fit to *ab initio* results obtained at the level of time-dependent-density functional theory (TD-DFT). We find that axially separated sp^3-defects are modeled well by this approximation and show

Scheme 1. Schematic of Transition Energy Diagram According to Kasha's Theory of HJ Aggregates, Where Both Monomers Are Identical (i.e., $\omega_i = \omega_j$) Producing Equal Exciton Splitting of $2J$[a]

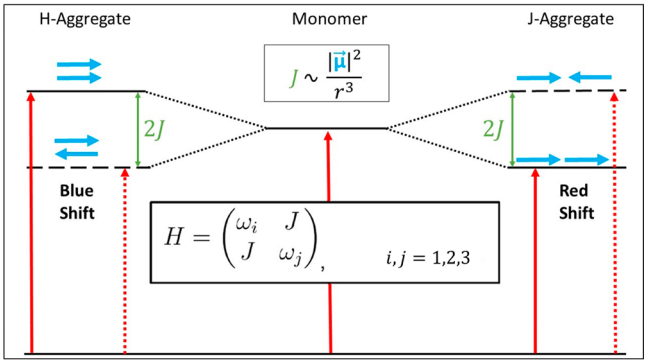

[a]H-aggregates are formed by stacking transition dipole moments, in this case of two monomers, producing a blue shifted bright transition relative to the transition of the monomer, since their lowest transition is optically inactive. J-aggregates are formed by a head-to-tail orientation of the transition dipole moments, which switches the optically bright and dark states, producing a red shifted transition.

qualitative correspondence to a model system with J-type aggregation for defect-associated states. However, circumferentially separated sp^3-defects do not display the corresponding H-type behavior of excitons. For closely packed paired sp^3-defects (separated by less than 2.5 nm), the defect−defect interaction has a reduced contribution of the dipole−dipole couplings and increased portion of exchange coupling due to stronger overlaps of defect-associated excitonic wave functions.[38,39] Defects placed along the circumference (in the supposed H-type orientation) demonstrate the strongest interaction among all considered geometries, where the dipole−dipole interactions are superseded by exchange due to the cylindrically diffusive character of exciton densities. In fact, this leads to the formation of a common potential energy well involving both defects which may host a manifold of excitonic states. Importantly, our calculations demonstrate that for the majority of interdefect orientations (the geometrical placement of the two defects with respect to one another), the lowest exciton remains optically bright, red-shifted from the main E_{11} band, and well-separated from the next optically dark state. All of these features are desirable for a strong emission in the near-infrared region. This implies that a selection of the defect type is not as critical for improving the emission efficiency of SWCNTs and that mixing of different types of defect pairs might be a promising direction for controlling efficient single-photon emission. Altogether, this work explains the recent experimental results, including the aforementioned DNA-wrapped SWCNTs[27,28] and high-resolution single-defect spectroscopy[26] in the context of defect−defect interactions.

Consistent with previous studies, our model consists of a single defect created by attaching two methyl groups bonded to adjacent carbon atoms of the SWCNT in one of three *ortho* configurations.[11,14,21] For any SWCNT, three *ortho* and three *para* configurations are available. In this work, we consider only defects of the *ortho* type, since it was shown to be a dominant binding configuration for (6,5) SWCNT.[9,11] Our results can be easily generalized for *para* defects as well. These three *ortho* positions include attachment of molecular adducts to two carbon atoms along the bond aligned with about 27°, 87°, and −33° from the tube axis. For brevity, these three *ortho* positions are named as 1, 2, and 3, respectively, Figure 1e and Figure S1, while their combinations (i.e., pairs of defects) will be denoted as C_{ij}. Each defect configuration has a unique redshift in energy from the main E_{11} transition corresponding

https://doi.org/10.1021/acs.jpclett.1c01631
J. Phys. Chem. Lett. 2021, 12, 7846−7853

to a unique degree of exciton wave function localization (ranging from 2 to 5 nm).[14] This dependence of the redshift on the localization can be thought of as varying depths of confining potential energy well hosting the excitons. Here, we focus on how these potential energy wells are coupled and modify the energy landscape and affect exciton localization.

Although there are numerous ways to orient/place a pair of sp^3-defects on the tube surface, we consider only three unique types of paired defects: (I) axial translations, where the axial separation between defects can be varied in terms of an integer n multiplying some length L (i.e., one-half of the circumference ~10 carbons ~1.3 nm) with n = 1, 2, 3, and 4, denoted as AxnL (Figure 1a,b); (II) circumferentially interacting defects, CircL (Figure 1c); and an angle-dependent interaction of both an axial and circumferential separation of sp^3-defects, AxL/CircL (Figure 1d). Each of these systems is defined as a combination of two independent *ortho* defects, e.g., C_{11}, C_{12}, C_{22}, C_{23}, C_{13}, and C_{33}.

The obtained ground state energies are analyzed to determine energetic stabilities of various pairs of defect configurations and optimal distances at which these defects interact, as shown in Figure 2. For uncoupled, noninteracting

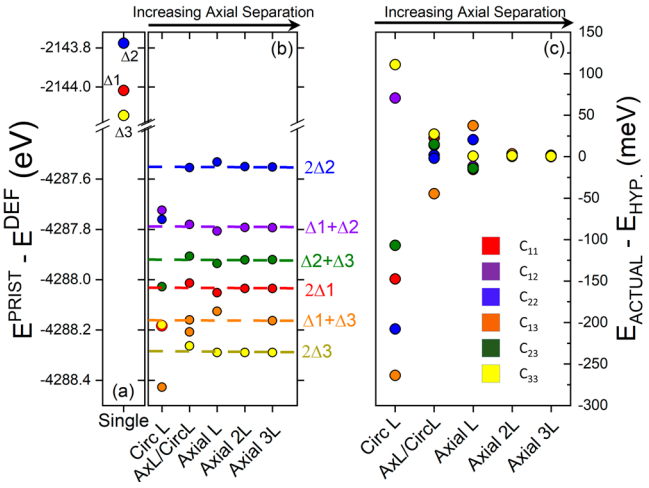

Figure 2. Thermodynamic stability of each defect geometry studied. (a) Single defect total energies are subtracted from those of pristine SWCNT, which we label Δ1, Δ2, and Δ3, respectively. (b) Paired defect total energies are subtracted from those of pristine SWCNT. The dashed lines represent different additive combinations of Δ1, Δ2, and Δ3 energies. For all defect pairs, a circumferential translation of length L (CircL) shows the strongest defect−defect interaction. The second column shows a combined axial translation of length L and a circumferential translation of length L (AxL/CircL), with the angle between defects and the tube axis at 45° (Figure 1d) . (c) The deviation from the additive hypothesis (dashed lines in part b). The relatively large spread in energies for the CircL defects implies that the energetic stability of the system strongly depends on the specific defect pairs, most likely a result of π-orbital resonance breaking. The limit of negligibly weak ground state interactions between the defect pairs is effectively reached at a separation of Axial 2L (~2.6 nm) and further reduced at Axial 3L.

defects, as is the case when the distance between defects is large (e.g., Ax3L ~4 nm), the stabilization energies, calculated as an energy difference between the pristine tube and the tube with paired sp^3-defects, show independent and additive character (Figure 2b,c). At this noninteracting limit, for example, the stabilization energy of a defect combination of type C_{31} could be well approximated by Δ3 + Δ1, where Δ3 and Δ1 are the differences between the total energy of the pristine SWCNT and the system with the singe defect of type-3 and type-1, respectively (dashed line in Figure 2b).

For each combination of defect pairs, energies noticeably deviate from the additive trend for the smallest axial separation, AxL, due to strong defect−defect interactions. While both AxL and CircL represent the same surface-bound separation length between defects, the largest deviation is observed for CircL defects, showing up to 260 meV in energy variations, Figure 2c. This deviation stems from the breaking of the short, circumferential π-orbital resonance paths in slightly different ways with each combination of defect types. Thus, all defect types at the CircL geometries are not independent, which implies a thermodynamic preference to form a specific nonfactorizable defect pair (i.e., highly overlapped wave functions) compared to interacting single defects.[11]

Despite the same axial separation of ~1.3 nm, the values of stabilization energies of AxL/CircL defects are different from the AxL defects (Figure 2b), while the magnitude of the deviations from the additive trend are nearly identical and is not larger than 50 meV for both cases (Figure 2c). This implies that the ground-state interaction only depends on the axial separation, while the details for each configuration may depend on other parameters. These other parameters include both geometric and π-orbital distortions as well as asymmetrical breaking of π-orbital resonance around the tube. This also points to a weak angular dependence based in π-orbital conjugation.

To model redshifts of excitons in structures with paired defects, one can write a simple Frenkel Exciton Hamiltonian (H) in the site basis for coupling of two sp^3-defects (or two interacting excitons, see Methodology and Scheme 1). For defect pairs consisting of two identical defect types (i = j), where $\omega_i = \omega_j = \omega$ is the exciton transition energy for a noninteracting single defect (e.g., commonly denoted in experiment as the E_{11}* or E_{11}^{*-} energy) and $J_{ij} = J_{ji} = J$ representing the coupling matrix element, Scheme 1. The resulting excitonic energies ($E_{\pm}$) of systems with interacting, identical paired defects are predicted to be shifted by J in the classical exciton model as $E_{\pm} = \omega \pm J$. For chemically nonidentical defects, where $\omega_i \neq \omega_j$, the exciton energies can be obtained by eq 2 (see Methodology). Quantum chemical calculations (here TD-DFT, see Methodology) allow convenient evaluation of all these quantities. For example, the simulation of individual defects results in ω_i and ω_j. The coupling matrix element, J can be estimated using a point-dipole approximation (eq 3 in Methodology) calculating interactions of two transition dipoles that are centered at the defects. Alternatively, J can be inferred from a splitting between states obtained from calculation of a defect pair. In this case, the electrostatic Coulomb component is evaluated beyond point-dipole approximations, and other contributions (such as exchange) are included as well.

Figure 3a shows the absorption spectra for C_{11} configurations at various axial defect−defect separation lengths (AxL−Ax3L) calculated by the linear response TD-DFT (see Methodology). In each case, the lowest-energy exciton is bright, and the second transition is dark, both shifted nearly symmetrically by about $\pm J$ with respect to the lowest exciton energy of the single defect system (the vertical blue line in Figure 3a). This agrees with predictions of eq 2 and eq 3 (with i = j): With increasing defect distance from L to 3L, we see a

https://doi.org/10.1021/acs.jpclett.1c01631
J. Phys. Chem. Lett. 2021, 12, 7846−7853

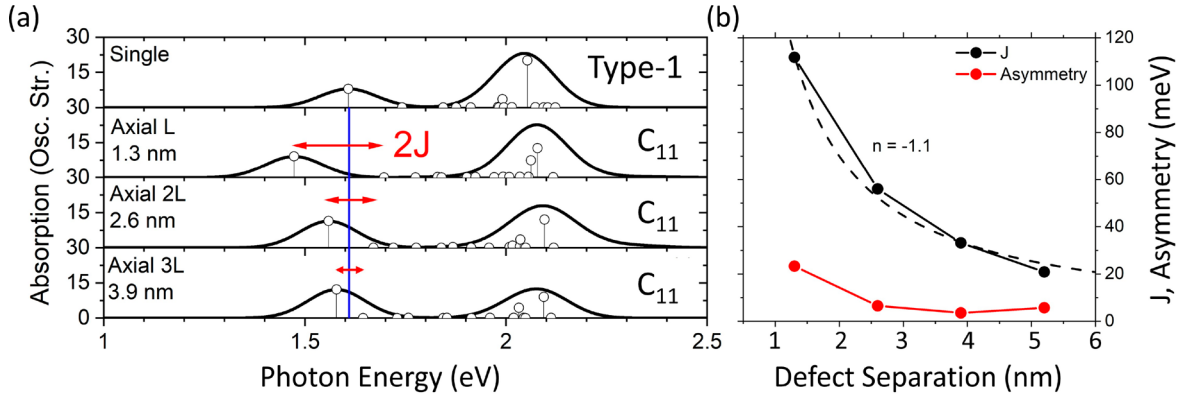

Figure 3. Characteristics of axial defect couplings in the excited state. (a) Absorption spectra of structures with an *ortho* defect of type-1 and axial defects composed of the same type, C_{11}, at various separations. The height of vertical gray lines with circles corresponds to the calculated oscillator strengths of optical transitions. The blue vertical line defines the lowest exciton energy for a single type-1 defect, as a reference for the *J*-coupling value. (b) *J*-coupling values for axial C_{11} defects as a function of defect−defect separation (solid black) calculated by eq 4. The dotted black line shows a power law fit to the data ($J \sim r^n$), with $n = -1.1 < -3$ showing a subdipole trend stemming from nonelectrostatic interactions such as exchange coupling. As the defects approach infinite separation length, each curve should approach zero for completely independent defects. The asymmetry of the splitting (solid red) estimated by eq 5 decreases with increasing distance, which helps characterize the amount of nonelectrostatic interactions at each separation length.

decrease both in the *J*-splitting magnitude (calculated by eq 4 in Methodology) and the *J*-splitting asymmetry (calculated by eq 5 in Methodology), Figure 3b. The splitting becomes more symmetric about the single defect transition with a larger defect separation because the excitons originating from each of the two defects become more spatially independent at larger distances, converging toward the ideal Kasha exciton model of J-aggregates (Scheme 1).[36] Note, a slight deviation from this trend (~5 meV) for the longest defect−defect separation, Ax4L, is due to finite-size effects, as the size of the single-defect excitonic wave functions encroach on the edge of the SWCNT and become slightly perturbed. Nonetheless, that magnitude of splitting, *J*, is negligibly affected by the finite-size effects.

The defect−defect coupling demonstrates a power law fit of $J \sim \mathrm{pow}(r,n)$ or r^n, where *r* is a defect−defect distance and $n = -1.1$, Figure 3b. This trend shows that the coupling decreases with increasing distance weaker (or "slower") than a pure dipole−dipole interaction, which scales like the inverse third power of separation length ($n = -3$). This deviation indicates that these nearby defects interact beyond point-dipole approximation and have other contributions such as exchange.[38] The latter stems directly from exciton wave function overlaps, which may be characterized by the asymmetry in the splitting (sometimes called the Dexter component).[40,41] While C_{11} configurations exhibit results mainly consistent with Kasha's model of J-aggregates, configurations C_{22} and C_{33} may require larger spatial separations to see ideal J-type splitting than computational resources allow due to their weakly localizing excitonic potential, as illustrated in Figures S2−S4, Table S1. Results for nonidentical defects $i \neq j$ are shown in Figures S5−S8.

Figure 4 shows transition densities of the two lowest excitons for six axial defect geometries illustrating the various interaction between defects according to the intrinsic properties of their trapping potential. All axial defects with at least one defect of type-1, the deepest potential well resulting in the most red-shifted exciton[14,22] (Table S1), demonstrate J-aggregate behavior where the first excited state is optically bright and the second state is optically dark due to their near-ideal dipole−dipole interactions (Figure S2). For nonidentical

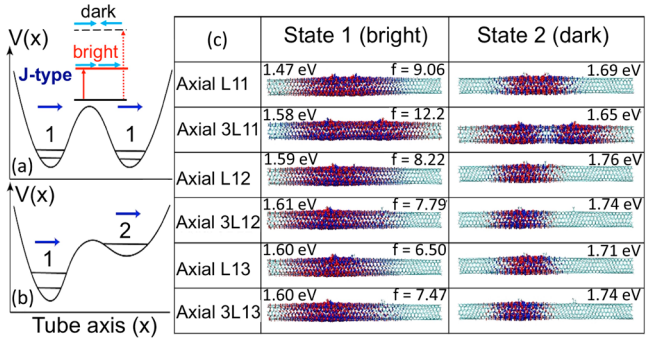

Figure 4. Schematic representation of the exciton potential well of interacting defects and calculated transition densities of two lowest excitons of several structures with axially paired defects. The excitonic potential, $V(x)$, for (a) two identical Axial defects C_{11} and (b) two different Axial defect types C_{12}, with both cases leading to the transition dipole moments acting as J-aggregates. (c) Transition densities of two lowest excitons for six Axial defect geometries, illustrating the various interaction between defects according to the intrinsic properties of their exciton potential wells, with all cases resulting in J-aggregates having optically bright first state (with oscillator strength *f* and transition energy listed inside each subpanel) and optically dark second state (where $f = 0.00$ in all cases).

axial defects, the exciton becomes trapped (or localized) within a single well due to the presence of a shallower trapping potential (Figure 4b). The exciton is shared, nearly equally, across wells for identical defects with identical trapping potentials (Figure 4a). For largely separated, identical defects, such as the Ax3L C_{11} case, the excitonic density is significantly reduced at the midpoint (or height of the potential barrier) between defects, pointing to weak overlap interactions and more dipolar J-type coupling. For largely separated, non-identical defects, the density for both states is attracted to the defect with the deepest trapping potential (i.e., the type-1 defect, Figure 4c). As a result, the defect pair C_{13} is the most coupled through electrostatics (the largest J-couplings, Figure S4b) and demonstrates large splitting between the first and second excitonic states (Figure S7). For example, the type-1 defect contains all of the density due to the large energy

https://doi.org/10.1021/acs.jpclett.1c01631
J. Phys. Chem. Lett. 2021, 12, 7846−7853

difference in potential well minima (Figure 4b). Similarly, the defect−defect interaction in the C_{12} system yields moderate J-couplings (Figure S4b) and exciton splitting (Figure S7) since the type-2 well is lower than type-3 (Table S1) but not as greatly separated in energy, allowing for more delocalization. Lastly, the defect−defect interaction in C_{23} weakly splits the two lowest states, since the type-3 and type-2 defects are both delocalized and hence have shallow effective wells, effectively causing the Kasha exciton model to break down (Table S1, Figures S4b and S7).

Overall, the nature of defect−defect interactions strongly depends on the depth of the trapping potential, revealing that dipole−dipole interactions dominate for systems involving deep potentials, and exchange couplings dominate in systems with shallow trapping potentials ($-3 < n < -1$ in $J \sim r^n$ fitting, Figure S4b), due to much stronger overlaps between their single-defect wave functions. Note that, for a single defect of type-3 (delocalized exciton), the optically bright, defect-originated state is energetically located above two, optically inactive states associated with the E_{11} pristine manifold (Figure S3) because the redshift from the E_{11} band is very small due to this defect's delocalized nature. While axial positions of identical defects of this type, C_{33}, insignificantly affect this alignment between bright and dark states, coupling of a type-3 defect with more localized defects (e.g., type-2 or type-1) changes this situation, making the lowest exciton bright and its properties governed by the nature of the most localized defect with the deeper trapping potential (Figures S5−S8). Overall, the mixture of nonidentical axial sp^3-defects is beneficial for emission, since the lowest excitonic state is always bright and well-split from the next optically dark state nearly independent of defect−defect distances (~0.1 eV for C_{13} and C_{12} defects), Figure 4c. Moreover, from six possible paired axial defects, half of them result in the most red-shifted bright exciton with nearly the same energy (defined by the defect of type-1 with the deepest trapping potential), when the defects are separated by more than 2.6 nm (2L). This is expected to affect the emission line width broadening to a smaller degree, compared to a spatially separated ensemble of the same types of single defects.

In addition to the distance dependence of defect−defect exciton splitting, we also characterize angular dependence of this interaction. This could be important since CircL defect orientations show the strongest thermodynamic stabilization for C_{13} and C_{11} combinations among all considered configurations, Figure 2b. These defects can, for example, be patterned with the DNA strands.[27,28] Figure 5 compares the *J*-couplings as a function of interaction angle θ for AxL/CircL defects of type C_{11}, which are estimated based on the splitting between the two lowest excited states obtained by TD-DFT calculations (eq 4, Methodology) and on the idealized effective model of single-defect transition dipoles (eq 2). Note that the angle $\theta = 0°$ corresponds to the axial defect AxL and $\theta = 90°$ corresponds to the CircL defect, as shown in Figure 1d. The values of *J*-couplings obtained from TD-DFT calculations of SWCNT with the AxL/CircL C_{11} defect follow the dipolar dependence on angle up to the boundary between H- and J-aggregates ($\theta = 54.7°$); after which, the *J*-coupling remains negative, strongly deviating from the ideal H-type curve, Figure 5. This deviation suggests that the paired defect at $\theta > 55°$ forms a new, hybrid defect, where the individual defects have lost their identities forming a single, shared confining potential (Figure 5, insert). This is because the excitonic density is

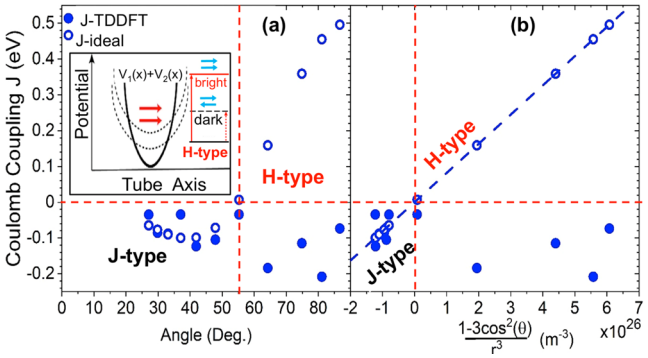

Figure 5. *J*-coupling values as functions of (a) angle and (b) an effective 1D parameter calculated from TD-DFT (filled circles) and from single-defect transition dipoles by eq 3 (empty circles) for AxL/CircL defects of type C_{11}. The inset shows schemes of the potential well, $V(x)$, for two CircL defects and the excitonic levels of the H-aggregate orientation. For the J-type regime (bounded by red dashed lines with $\theta < 54.7° = \theta_C$), there is qualitative agreement between the methods. In contrast, the H-type aggregates break down in this comparison, as the systems never produce H-type splitting for $\theta > \theta_C$.

nearly equally distributed about the SWCNT circumference, which can be clearly seen in Figure 4c and Table S2.

As a final note, we examine the symmetry of the shape of the transition density originating from each defect. Interestingly, the lower-energy state always corresponds to the J-type aggregate symmetry (see Table S2 for C_{11} defects and the corresponding reduced model system in Table S3, Figures S12 and S13). This implies that each defect still retains at least some portion of their weakly interacting characteristics, even with largely overlapping wave functions, to retain the parallel/antiparallel linear combination of transition dipoles. This partial J-behavior is also evidenced by the fact that the lowest exciton is optically bright for all AxL/CircL defects with $\theta < 54.7°$ (Figure S10) and CircL defects ($\theta = 90°$) involving at least one defect of type-1 with the deepest trapping potential (Figure S11). However, defects with shallow trapping potentials result in higher energy of the lowest exciton than those of a single defect, with CircL and AxL/CircL C_{13} defects being optically bright, while CircL C_{22}, C_{12}, and C_{33} are optically dark. Such a strong discrepancy between TD-DFT calculations and the simple point-dipole model is due to increased spatial extent of excitons associated with the shallow trapping potential of defects, which makes the exchange interaction dominant over direct electrostatic interactions. Nonetheless, for a vast majority of paired defects with circumferential placement, the lowest excitonic state is optically bright, red-shifted from the main E_{11} band, and well-separated from the next optically inactive state, with all these features favoring emission of SWCNTs.

In conclusion, we have explored the interaction between spatially localized sp^3-hybridized defects in SWCNTs using TD-DFT and have shown that their interaction conforms to the well-known Frenkel Exciton model describing, for example, electronic features of H and J molecular aggregates in the case of axially well-spaced defects (>2 nm). For axially spaced defects, J-aggregate behavior dominates. This results in separation between the lowest energy optically bright exciton and the next optically dark exciton. This separation reduces with increasing distance between defects from ~100 meV at ~2 nm down to ~30 meV (being on the order of thermal fluctuations) at ~5 nm distance. However, the energy splitting

https://doi.org/10.1021/acs.jpclett.1c01631
J. Phys. Chem. Lett. 2021, 12, 7846−7853

between two lowest bright and dark excitons stays maximal (>100 meV at 5 nm distance) for the mixture of two different defect types with one having the deepest trapping potential. In the short-distance limit (~1.3 nm), we found that the defects are coupled beyond classical dipole−dipole interactions and can no longer be considered as factorizable linear combinations of individual defect wave functions. This trend is the most pronounced for circumferential placement of paired defects due to their diffusive and overlapping character of the defect-associated wave functions, where the exchange coupling plays a leading role in the defect−defect interactions. However, even in this regime, the lowest exciton stays optically bright and well-separated from the next dark exciton for the vast majority of defect configurations considered. The redshift of the bright defect-based exciton from the main E_{11} band of the pristine SWCNT is governed by the defect with the deepest trapping potential, while typically being larger (more extended along the axis) compared to the exciton originating from a single defect.

Overall, our computational results address the challenge of selectivity of the defect-based emissive state in functionalized SWCNTs. We have shown that two different sp^3-defects placed at the SWCNT surface mostly do not change the ordering between the lowest optically bright and dark excitons, leaving the lowest state bright. Importantly, its energy splitting from the dark exciton and the main E_{11} band can be tuned through control of the axial separation between adjacent defect sites. Such control over defect separation has been recently realized experimentally through ss-DNA-wrapped SWCNTs.[27,28] The gained knowledge of how defects interact suggests many-fold impact: (i) new direction of synthetic control via coupled defects, (ii) further guideline in the tunability of the low-energy emissive states in functionalized SWCNTs, and (iii) clarification of open experimental questions, such as exciton trapping and interacting photon emitters in correlation experiments.[12,24,42]

METHODOLOGY

Quantum-Chemical Calculations. The calculations are carried out on a finite (6,5) SWCNT of three unit cells in length (~12 nm) capped with hydrogen atoms. This capping scheme was found to successfully reproduce the electronic structure of the infinite (6,5) SWCNT.[43] These SWCNT structures with single and paired sp^3-defects are optimized with density functional theory (DFT) using the CAM-B3LYP functional and STO-3G basis set, as implemented in Gaussian 16 software.[44] This methodology was previously shown to recover the electronic localization for both pristine and functionalized tubes and be consistent with experimental observations.[9,11,14,43] We use the same functional and basis set for excited state time-dependent DFT (TD-DFT) as for the ground state calculations. This level of theory has been shown to reproduce reasonable exciton size distributions and emission energies of functionalized SWCNTs comparable to experimental data.[3,15,43]

Frenkel Exciton Model. One can write down an effective Hamiltonian in the site basis coupling two defects (i.e., excitons) as

$$H = \begin{pmatrix} \omega_i & J_{ij} \\ J_{ij} & \omega_j \end{pmatrix}, \quad i, j = 1, 2, 3 \tag{1}$$

where ω_i is the transition energy for a noninteracting defect of configuration i (see Figure 1 for definition of configuration) and J_{ij} is the Coulomb coupling between the defects. In the most general case, the defects are not chemically identical and have spectrally dissimilar transition energies ($\omega_i \neq \omega_j$). Transition energies of the resulting excitonic states are eigenvalues of eq 1 and given by

$$E_{\pm} = \frac{\omega_i + \omega_j}{2} \pm \sqrt{\left(\frac{\omega_i - \omega_j}{2}\right)^2 + J_{ij}^2} \tag{2}$$

In order to describe the Coulomb coupling between sites, it is common to employ a point-dipole approximation such that

$$J_{ij} = \frac{1}{4\pi\varepsilon_o} \frac{\vec{\mu}_i \cdot \vec{\mu}_j - (\vec{\mu}_i \cdot \hat{r})(\vec{\mu}_j \cdot \hat{r})}{|\vec{r}|^3} \tag{3}$$

where $\vec{\mu}_i$ is the transition dipole moment of noninteracting defect i and $\vec{r}$ is a vector connecting the center of masses of each defect. This point dipole approximation is valid for dipoles that are small compared to the dipole−dipole separation distance. The orientation of the transition dipole moments influences J_{ij}, which ultimately determines the energies and oscillator strengths of the excitonic states.

The model can be derived from first-principle calculations of the excited state of the functionalized SWCNT. The lowest optical transition energies for the SWCNT with a single defect and pair of defects are computed by TDDFT and denoted as E_S for a single defect, and E_- and E_+ for the first and second optical transitions of the paired defects, so that $E_- < E_S < E_+$, as depicted in Figure 3a and Figures S2 and S3. For numerical analysis of defect−defect couplings for different separations between axial defects of the same type, we use the following linear combinations of transition energies as a measure of exciton−exciton interaction:

$$J = \frac{E_+ - E_-}{2} \tag{4}$$

A measure of asymmetry between the first two excitons associated with the paired identical defects with respect to the reference point of the lowest exciton of a single defect is defined as

$$\text{asymmetry} = \frac{(E_+ - E_S) - (E_S - E_-)}{2} \tag{5}$$

The values of J and asymmetry are shown in Figure 3b by black and red lines, respectively. For nonidentical defects, Figure S4, eq 2 is used to calculate coupling strengths, and a similar expression to eq 5 is used to calculate the asymmetry.

Two typical classes of systems are known as H- and J-aggregates (Figure 1e). For the J-type geometry ($J_{ij} < 0$), transition dipoles are aligned in a head-to-tail orientation (i.e., → →), and the bright state is red-shifted relative to the monomer's transition energy. For the H-type geometry ($J_{ij} > 0$), the dipoles are stacked, and the bright state is blue-shifted relative to the monomer's transition energy.

ASSOCIATED CONTENT

Supporting Information

The Supporting Information is available free of charge at https://pubs.acs.org/doi/10.1021/acs.jpclett.1c01631.

Array of spectra for all geometries studied in this work, real-space projected transition density for single-defect and angular-dependent geometries, as well as an analysis of a model HJ-aggregate system (PDF)

https://doi.org/10.1021/acs.jpclett.1c01631
J. Phys. Chem. Lett. 2021, 12, 7846−7853

AUTHOR INFORMATION

Corresponding Author

Sergei Tretiak − *Center for Integrated Nanotechnologies, Center for Nonlinear Studies, and Theoretical Division Los Alamos National Laboratory, Los Alamos, New Mexico 87545, United States;* orcid.org/0000-0001-5547-3647; Email: serg@lanl.gov

Authors

Braden M. Weight − *Center for Integrated Nanotechnologies, Center for Nonlinear Studies, and Theoretical Division Los Alamos National Laboratory, Los Alamos, New Mexico 87545, United States; Department of Physics and Astronomy, University of Rochester, Rochester, New York 14627, United States; Department of Chemistry and Biochemistry and Department of Physics, North Dakota State University, Fargo, North Dakota 58102, United States;* orcid.org/0000-0002-2441-3569

Andrew E. Sifain − *U.S. Army Research Laboratory, Aberdeen Proving Ground, Maryland 21005, United States;* orcid.org/0000-0002-2964-1923

Brendan J. Gifford − *Center for Integrated Nanotechnologies, Center for Nonlinear Studies, and Theoretical Division Los Alamos National Laboratory, Los Alamos, New Mexico 87545, United States;* orcid.org/0000-0002-4116-711X

Dmitri Kilin − *Department of Chemistry and Biochemistry, North Dakota State University, Fargo, North Dakota 58102, United States;* orcid.org/0000-0001-7847-5549

Svetlana Kilina − *Department of Chemistry and Biochemistry, North Dakota State University, Fargo, North Dakota 58102, United States;* orcid.org/0000-0003-1350-2790

Complete contact information is available at: https://pubs.acs.org/10.1021/acs.jpclett.1c01631

Notes

The authors declare no competing financial interest.

ACKNOWLEDGMENTS

S.K. thanks the financial support of DOE EPSCoR: Building EPSCoR-State/National Laboratory Partnerships Grant No. DE-SC0021287. D.K. acknowledges support of NSF CHE-1944921. For computational resources and administrative support, the authors thank the Center for Computationally Assisted Science and Technology (CCAST) at North Dakota State University and the National Energy Research Scientific Computing Center (NERSC) Allocation Award 86678, supported by the Office of Science of the DOE under Contract No. DE-AC02-05CH11231. This work was performed in part at the Center for Integrated Nanotechnology (CINT) and Center for Nonlinear Studies (CNLS), U.S. Department of Energy and Office of Basic Energy Sciences user facilities and supported by the Los Alamos National Laboratory (LANL) Directed Research and Development funds (LDRD).

REFERENCES

(1) Perebeinos, V.; Tersoff, J.; Avouris, P. Scaling of Excitons in Carbon Nanotubes. *Phys. Rev. Lett.* **2004**, *92* (25), 257402.

(2) Kilina, S.; Badaeva, E.; Piryatinski, A.; Tretiak, S.; Saxena, A.; Bishop, A. R. Bright and Dark Excitons in Semiconductor Carbon Nanotubes: Insights from Electronic Structure Calculations. *Phys. Chem. Chem. Phys.* **2009**, *11* (21), 4113−4123.

(3) Kilina, S.; Ramirez, J.; Tretiak, S. Brightening of the Lowest Exciton in Carbon Nanotubes via Chemical Functionalization. *Nano Lett.* **2012**, *12* (5), 2306−2312.

(4) Zhou, W.; Nakamura, D.; Liu, H.; Kataura, H.; Takeyama, S. Relative Ordering between Bright and Dark Excitons in Single-Walled Carbon Nanotubes. *Sci. Rep.* **2015**, *4* (1), 6999.

(5) Lüer, L.; Hoseinkhani, S.; Polli, D.; Crochet, J.; Hertel, T.; Lanzani, G. Size and Mobility of Excitons in (6, 5) Carbon Nanotubes. *Nat. Phys.* **2009**, *5* (1), 54−58.

(6) Glückert, J. T.; Adamska, L.; Schinner, W.; Hofmann, M. S.; Doorn, S. K.; Tretiak, S.; Högele, A. Dipolar and Charged Localized Excitons in Carbon Nanotubes. *Phys. Rev. B: Condens. Matter Mater. Phys.* **2018**, *98* (19), 195413.

(7) Tretiak, S.; Kilina, S.; Piryatinski, A.; Saxena, A.; Martin, R. L.; Bishop, A. R. Excitons and Peierls Distortion in Conjugated Carbon Nanotubes. *Nano Lett.* **2007**, *7* (1), 86−92.

(8) Kim, Y.; Goupalov, S. V.; Weight, B. M.; Gifford, B. J.; He, X.; Saha, A.; Kim, M.; Ao, G.; Wang, Y.; Zheng, M.; Tretiak, S.; Doorn, S. K.; Htoon, H. Hidden Fine Structure of Quantum Defects Revealed by Single Carbon Nanotube Magneto-Photoluminescence. *ACS Nano* **2020**, *14* (3), 3451−3460.

(9) Saha, A.; Gifford, B. J.; He, X.; Ao, G.; Zheng, M.; Kataura, H.; Htoon, H.; Kilina, S.; Tretiak, S.; Doorn, S. K. Narrow-Band Single-Photon Emission through Selective Aryl Functionalization of Zigzag Carbon Nanotubes. *Nat. Chem.* **2018**, *10* (11), 1089−1095.

(10) Kwon, H.; Furmanchuk, A.; Kim, M.; Meany, B.; Guo, Y.; Schatz, G. C.; Wang, Y. Molecularly Tunable Fluorescent Quantum Defects. *J. Am. Chem. Soc.* **2016**, *138* (21), 6878−6885.

(11) Gifford, B. J.; He, X.; Kim, M.; Kwon, H.; Saha, A.; Sifain, A. E.; Wang, Y.; Htoon, H.; Kilina, S.; Doorn, S. K.; Tretiak, S. Optical Effects of Divalent Functionalization of Carbon Nanotubes. *Chem. Mater.* **2019**, *31* (17), 6950−6961.

(12) He, X.; Sun, L.; Gifford, B. J.; Tretiak, S.; Piryatinski, A.; Li, X.; Htoon, H.; Doorn, S. K. Intrinsic Limits of Defect-State Photoluminescence Dynamics in Functionalized Carbon Nanotubes. *Nanoscale* **2019**, *11* (18), 9125−9132.

(13) He, X.; Velizhanin, K. A.; Bullard, G.; Bai, Y.; Olivier, J.-H.; Hartmann, N. F.; Gifford, B. J.; Kilina, S.; Tretiak, S.; Htoon, H.; Therien, M. J.; Doorn, S. K. Solvent- and Wavelength-Dependent Photoluminescence Relaxation Dynamics of Carbon Nanotube Sp3 Defect States. *ACS Nano* **2018**, *12* (8), 8060−8070.

(14) Gifford, B. J.; Kilina, S.; Htoon, H.; Doorn, S. K.; Tretiak, S. Exciton Localization and Optical Emission in Aryl-Functionalized Carbon Nanotubes. *J. Phys. Chem. C* **2018**, *122* (3), 1828−1838.

(15) Gifford, B. J.; Sifain, A. E.; Htoon, H.; Doorn, S. K.; Kilina, S.; Tretiak, S. Correction Scheme for Comparison of Computed and Experimental Optical Transition Energies in Functionalized Single-Walled Carbon Nanotubes. *J. Phys. Chem. Lett.* **2018**, *9* (10), 2460−2468.

(16) Endo, T.; Ishi-Hayase, J.; Maki, H. Photon Antibunching in Single-Walled Carbon Nanotubes at Telecommunication Wavelengths and Room Temperature. *Appl. Phys. Lett.* **2015**, *106* (11), 113106.

(17) He, X.; Htoon, H.; Doorn, S. K.; Pernice, W. H. P.; Pyatkov, F.; Krupke, R.; Jeantet, A.; Chassagneux, Y.; Voisin, C. Carbon Nanotubes as Emerging Quantum-Light Sources. *Nat. Mater.* **2018**, *17* (8), 663−670.

(18) Ma, X.; Hartmann, N. F.; Baldwin, J. K. S.; Doorn, S. K.; Htoon, H. Room-Temperature Single-Photon Generation from Solitary Dopants of Carbon Nanotubes. *Nat. Nanotechnol.* **2015**, *10* (8), 671−675.

(19) Slussarenko, S.; Pryde, G. J. Photonic Quantum Information Processing: A Concise Review. *Appl. Phys. Rev.* **2019**, *6* (4), 041303.

(20) Gifford, B. J.; Saha, A.; Weight, B. M.; He, X.; Ao, G.; Zheng, M.; Htoon, H.; Kilina, S.; Doorn, S. K.; Tretiak, S. Mod(n-m,3) Dependence of Defect-State Emission Bands in Aryl-Functionalized Carbon Nanotubes. *Nano Lett.* **2019**, *19* (12), 8503−8509.

(21) Weight, B. M.; Gifford, B. J.; Tretiak, S.; Kilina, S. Interplay between Electrostatic Properties of Molecular Adducts and Their

Positions at Carbon Nanotubes. *J. Phys. Chem. C* **2021**, *125* (8), 4785−4793.
(22) He, X.; Gifford, B. J.; Hartmann, N. F.; Ihly, R.; Ma, X.; Kilina, S. V.; Luo, Y.; Shayan, K.; Strauf, S.; Blackburn, J. L.; Tretiak, S.; Doorn, S. K.; Htoon, H. Low-Temperature Single Carbon Nanotube Spectroscopy of Sp ^{3} Quantum Defects. *ACS Nano* **2017**, *11* (11), 10785−10796.
(23) Zheng, Y.; Bachilo, S. M.; Weisman, R. B. Photoexcited Aromatic Reactants Give Multicolor Carbon Nanotube Fluorescence from Quantum Defects. *ACS Nano* **2020**, *14* (1), 715−723.
(24) Kim, Y.; Velizhanin, K. A.; He, X.; Sarpkaya, I.; Yomogida, Y.; Tanaka, T.; Kataura, H.; Doorn, S. K.; Htoon, H. Photoluminescence Intensity Fluctuations and Temperature-Dependent Decay Dynamics of Individual Carbon Nanotube Sp3 Defects. *J. Phys. Chem. Lett.* **2019**, *10* (6), 1423−1430.
(25) Saha, A.; Gifford, B. J.; He, X.; Ao, G.; Zheng, M.; Kataura, H.; Htoon, H.; Kilina, S.; Tretiak, S.; Doorn, S. K. Narrow-Band Single-Photon Emission through Selective Aryl Functionalization of Zigzag Carbon Nanotubes. *Nat. Chem.* **2018**, *10* (11), 1089−1095.
(26) Wu, X.; Kim, M.; Qu, H.; Wang, Y. Single-Defect Spectroscopy in the Shortwave Infrared. *Nat. Commun.* **2019**, *10* (1), 1−7.
(27) Zheng, Y.; Bachilo, S. M.; Weisman, R. B. Controlled Patterning of Carbon Nanotube Energy Levels by Covalent DNA Functionalization. *ACS Nano* **2019**, *13* (7), 8222−8228.
(28) Zheng, Y.; Weight, B. M.; Jones, A. C.; Chandrasekaran, V.; Gifford, B. J.; Tretiak, S.; Doorn, S. K.; Htoon, H. Photoluminescence Dynamics Defined by Exciton Trapping Potential of Coupled Defect States in DNA-Functionalized Carbon Nanotubes. *ACS Nano* **2021**, *15* (1), 923−933.
(29) Wong, C. Y.; Curutchet, C.; Tretiak, S.; Scholes, G. D. Ideal Dipole Approximation Fails to Predict Electronic Coupling and Energy Transfer between Semiconducting Single-Wall Carbon Nanotubes. *J. Chem. Phys.* **2009**, *130* (8), 081104.
(30) Tretiak, S. Triplet State Absorption in Carbon Nanotubes: A TD−DFT Study. *Nano Lett.* **2007**, *7* (8), 2201−2206.
(31) Tretiak, S.; Mukamel, S. Density Matrix Analysis and Simulation of Electronic Excitations in Conjugated and Aggregated Molecules. *Chem. Rev.* **2002**, *102* (9), 3171−3212.
(32) Capaz, R. B.; Spataru, C. D.; Ismail-Beigi, S.; Louie, S. G. Diameter and Chirality Dependence of Exciton Properties in Carbon Nanotubes. *Phys. Rev. B: Condens. Matter Mater. Phys.* **2006**, *74* (12), 121401.
(33) Dvorak, M.; Wei, S.-H.; Wu, Z. Origin of the Variation of Exciton Binding Energy in Semiconductors. *Phys. Rev. Lett.* **2013**, *110* (1), 016402.
(34) Miyauchi, Y.; Iwamura, M.; Mouri, S.; Kawazoe, T.; Ohtsu, M.; Matsuda, K. Brightening of Excitons in Carbon Nanotubes on Dimensionality Modification. *Nat. Photonics* **2013**, *7* (9), 715−719.
(35) Stich, D.; Späth, F.; Kraus, H.; Sperlich, A.; Dyakonov, V.; Hertel, T. Triplet−Triplet Exciton Dynamics in Single-Walled Carbon Nanotubes. *Nat. Photonics* **2014**, *8* (2), 139−144.
(36) Kasha, M.; Rawls, H. R.; Ashraf El-Bayoumi, M. The Exciton Model in Molecular Spectroscopy. *Pure Appl. Chem.* **1965**, *11*, 371−592.
(37) Kasha, M. Energy Transfer Mechanisms and the Molecular Exciton Model for Molecular Aggregates. *Radiat. Res.* **1963**, *20* (1), 55−70.
(38) Hestand, N. J.; Spano, F. C. Expanded Theory of H- and J-Molecular Aggregates: The Effects of Vibronic Coupling and Intermolecular Charge Transfer. *Chem. Rev.* **2018**, *118* (15), 7069−7163.
(39) Hestand, N. J.; Spano, F. C. Molecular Aggregate Photophysics beyond the Kasha Model: Novel Design Principles for Organic Materials. *Acc. Chem. Res.* **2017**, *50* (2), 341−350.
(40) Dexter, D. L. A Theory of Sensitized Luminescence in Solids. *J. Chem. Phys.* **1953**, *21* (5), 836−850.
(41) Thompson, A. L.; Gaab, K. M.; Xu, J.; Bardeen, C. J.; Martínez, T. J. Variable Electronic Coupling in Phenylacetylene Dendrimers: The Role of Förster, Dexter, and Charge-Transfer Interactions. *J. Phys. Chem. A* **2004**, *108* (4), 671−682.
(42) Nutz, M.; Zhang, J.; Kim, M.; Kwon, H.; Wu, X.; Wang, Y.; Högele, A. Photon Correlation Spectroscopy of Luminescent Quantum Defects in Carbon Nanotubes. *Nano Lett.* **2019**, *19* (10), 7078−7084.
(43) Sharma, A.; Gifford, B. J.; Kilina, S. Tip Functionalization of Finite Single-Walled Carbon Nanotubes and Its Impact on the Ground and Excited State Electronic Structure. *J. Phys. Chem. C* **2017**, *121* (15), 8601−8612.
(44) Frisch, M. J.; Trucks, G. W.; Schlegel, H. B.; Scuseria, G. E.; Robb, M. A.; Cheeseman, J. R.; Scalmani, G.; Barone, V.; Petersson, G. A.; Nakatsuji, H.; Li, X.; Caricato, M.; Marenich, A. V.; Bloino, J.; Janesko, B. G.; Gomperts, R.; Mennucci, B.; Hratchian, H. P.; Ortiz, J. V.; Izmaylov, A. F.; Sonnenberg, J. L.; Williams; Ding, F.; Lipparini, F.; Egidi, F.; Goings, J.; Peng, B.; Petrone, A.; Henderson, T.; Ranasinghe, D.; Zakrzewski, V. G.; Gao, J.; Rega, N.; Zheng, G.; Liang, W.; Hada, M.; Ehara, M.; Toyota, K.; Fukuda, R.; Hasegawa, J.; Ishida, M.; Nakajima, T.; Honda, Y.; Kitao, O.; Nakai, H.; Vreven, T.; Throssell, K.; Montgomery, J. A., Jr.; Peralta, J. E.; Ogliaro, F.; Bearpark, M. J.; Heyd, J. J.; Brothers, E. N.; Kudin, K. N.; Staroverov, V. N.; Keith, T. A.; Kobayashi, R.; Normand, J.; Raghavachari, K.; Rendell, A. P.; Burant, J. C.; Iyengar, S. S.; Tomasi, J.; Cossi, M.; Millam, J. M.; Klene, M.; Adamo, C.; Cammi, R.; Ochterski, J. W.; Martin, R. L.; Morokuma, K.; Farkas, O.; Foresman, J. B.; Fox, D. J. *Gaussian 16*, Rev. C.01; Gaussian Inc.: Wallingford, CT, 2016.

https://doi.org/10.1021/acs.jpclett.1c01631
J. Phys. Chem. Lett. 2021, 12, 7846−7853